













Bosonic condensation of exciton–polaritons in an atomically thin crystal

Carlos Anton-Solanas^{1,2,12}  , Maximilian Waldherr^{1,12}, Martin Klaas¹, Holger Suchomei¹, Tristan H. Harder¹ , Hui Cai³, Evgeny Sedov^{4,5,6} , Sebastian Klemmt¹ , Alexey V. Kavokin^{4,5,7} , Sefaattin Tongay⁸ , Kenji Watanabe⁹ , Takashi Taniguchi¹⁰ , Sven Höfling^{1,11}  and Christian Schneider² 

The emergence of two-dimensional crystals has revolutionized modern solid-state physics. From a fundamental point of view, the enhancement of charge carrier correlations has sparked much research activity in the transport and quantum optics communities. One of the most intriguing effects, in this regard, is the bosonic condensation and spontaneous coherence of many-particle complexes. Here we find compelling evidence of bosonic condensation of exciton–polaritons emerging from an atomically thin crystal of MoSe₂ embedded in a dielectric microcavity under optical pumping at cryogenic temperatures. The formation of the condensate manifests itself in a sudden increase of luminescence intensity in a threshold-like manner, and a notable spin-polarizability in an externally applied magnetic field. Spatial coherence is mapped out via highly resolved real-space interferometry, revealing a spatially extended condensate. Our device represents a decisive step towards the implementation of coherent light-sources based on atomically thin crystals, as well as non-linear, valleytronic coherent devices.

Bose–Einstein condensation represents a non-classical phase transition, characterized by the collapse of an ensemble of quantum particles into a macroscopic and coherent state. Experimentally, the investigation of Bose–Einstein condensates was pioneered in the field of ultracold atoms^{1,2}. However, it was early on proposed³, and subsequently verified, that bosonic many-body excitations in solids⁴, including excitons and exciton–polaritons, are capable of forming non-equilibrium condensates at relatively high temperatures, which makes them a more user-friendly system for such fundamental studies. The solid-state, ‘on-chip’ character intrinsically offers a degree of practicality, and the fact that excitons and exciton–polaritons emit light makes their condensates of great appeal in the application-driven research for novel and innovative light sources^{5,6}, as well as in the field of non-linear photonics⁷. The latter is particularly relevant for the case of exciton–polaritons formed in high-quality microcavities loaded with active materials in the strong light–matter coupling regime⁸.

The non-linear character, as well as the spinor properties which dominate the condensation behaviour of exciton–polaritons and affect their intrinsic properties, are strongly linked to the materials embedded in the microcavities. Recently, atomically thin crystals of transition metal dichalcogenides (TMDCs) have emerged as a new, compelling platform in solid-state-based cavity quantum electrodynamics⁹, benefiting from ultrastable excitons¹⁰, giant oscillator strength, and exotic polarization and topological properties.

A variety of reports have now addressed the emergence of exciton–polaritons with single and multiple TMDC crystals^{11–14} embedded in high-quality-factor microcavities. Aspects associated with

the valley character of excitons in TMDC layers in the strong coupling regime have also been demonstrated^{15,16}. However, despite recent discoveries of strong non-linearities of TMDC excitons^{17–19}, phenomena related to bosonic condensation of exciton–polaritons with TMDC crystals remain unaddressed. Hints of bosonic condensates of bare excitons in TMDC van der Waals heterostructures were recently reported²⁰; however, the strong inhomogeneities of the utilized samples prohibited the exploration of spatially extended coherent states.

In this article we report the emergence of a coherent condensate of exciton–polaritons in a microcavity loaded with a single crystal of monolayer MoSe₂. Our device, which is operated at cryogenic temperatures (4 K), features the sharp non-linear threshold characteristic of a polariton laser and demonstrates a strong valley polarization in an externally applied magnetic field in the regime of bosonic condensation. Finally, we observe distinct features of spatial coherence via classic interferometry.

Sample structure

The studied sample structure is schematically depicted in Fig. 1a. It is based on a hybrid III/V dielectric cavity, which was assembled mechanically. The bottom distributed Bragg reflector (DBR), which was grown by molecular beam epitaxy, consists of 24 AlAs/Al_{0.2}Ga_{0.8}As mirror pairs with thicknesses of 62 and 53 nm, respectively, and features a stop band centred around 753 nm. A 52-nm-thick AlAs spacer forms the lower half of the optical cavity. The spacer is capped by a 3-nm-thick GaAs capping layer and features a heavily doped, 4.75-nm-thick GaAs quantum well (QW)

¹Technische Physik and Würzburg–Dresden Cluster of Excellence ct.qmat, Universität Würzburg, Würzburg, Germany. ²Institute of Physics, Carl von Ossietzky University, Oldenburg, Germany. ³University of California, Merced, Merced, CA, USA. ⁴School of Science, Westlake University, Hangzhou, P. R. China. ⁵Institute of Natural Sciences, Westlake Institute for Advanced Study, Hangzhou, P. R. China. ⁶Vladimir State University named after A.G. and N.G. Stoletovs, Vladimir, Russia. ⁷Spin Optics Laboratory, St Petersburg State University, St Petersburg, Russia. ⁸School for Engineering of Matter, Transport, and Energy, Arizona State University, Tempe, AZ, USA. ⁹Research Center for Functional Materials, National Institute for Materials Science, Tsukuba, Japan. ¹⁰International Center for Materials Nanoarchitectonics, National Institute for Materials Science, Tsukuba, Japan. ¹¹SUPA, School of Physics and Astronomy, University of St Andrews, St Andrews, UK. ¹²These authors contributed equally: C. Anton-Solanas, M. Waldherr.

✉e-mail: carlos.anton-solanas@uni-oldenburg.de; Sefaattin.Tongay@asu.edu; christian.schneider@uni-oldenburg.de

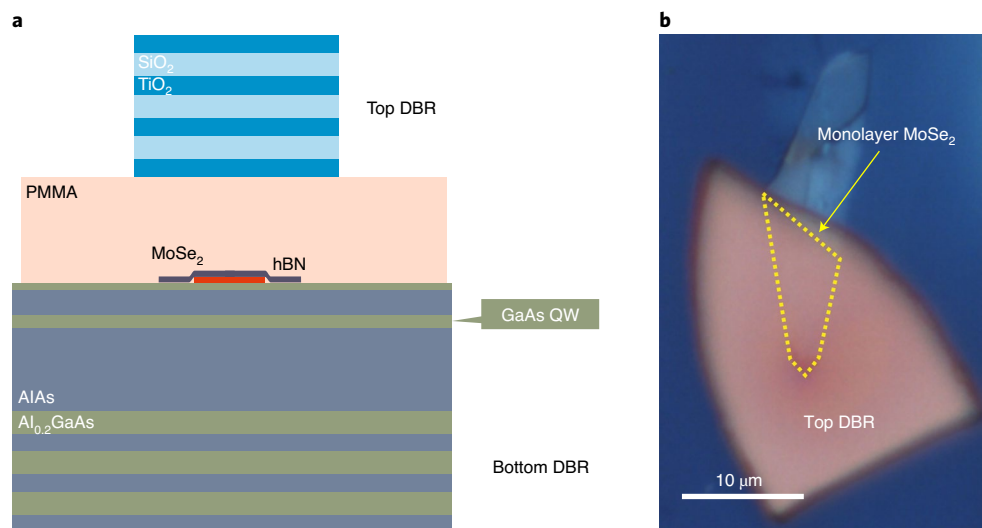


Fig. 1 | Sample structure and map. **a**, Schematic drawing of the microcavity structure. The lower DBR was grown epitaxially. The MoSe₂ layer is covered by a thin layer of hBN and a layer of PMMA that acts as a spacer. The top DBR is composed of 8.5 pairs of TiO₂/SiO₂ and was mechanically separated from a carrier substrate and transferred on top of the PMMA (see details in the text and Methods). **b**, Microscope image of the full structure. The position of the monolayer underneath the top DBR is schematically indicated by the dotted yellow line.

located 10 nm underneath the surface. The inclusion of GaAs layers in the heterostructures substantially improves the crystal quality at the GaAs/TMDC interface, and provides access to carriers to enhance polariton–electron scattering processes.

Electron–polariton scattering has been identified as an efficient mechanism to promote the condensation of exciton–polaritons^{21,22}. More recently, it was found that strongly charged exciton–polaritons in TMDC microcavities display remarkably enhanced gain in ultra-fast studies compared with the uncharged case²³.

Next, an atomically thin layer of MoSe₂, isolated from a bulk crystal grown by chemical vapour deposition is transferred onto the bottom DBR via a dry-gel stamping method²⁴. This layer is subsequently capped by a thin layer of hexagonal boron nitride (hBN). Then, we spin-coated an ~90-nm-thick polymethyl methacrylate (PMMA) buffer layer, forming the upper half of the cavity. Finally, a piece of a separate SiO₂/TiO₂ DBR with lateral dimensions of a few tens of μm (composed by 8.5 pairs, stop band centre at 750 nm, terminated by TiO₂ on both sides) is mechanically peeled off its substrate and transferred onto the buffer layer by the same dry-gel method, concluding the heterostructure sketched in Fig. 1a. Figure 1b shows a microscope image of the final structure (top view), where the contour of the MoSe₂ monolayer (4 μm × 12 μm) is marked by the yellow dotted line.

Dispersion relation and detuning characteristics

We study our sample at a temperature of 4 K via momentum-resolved micro-photoluminescence spectroscopy²⁵ in the back-Fourier plane imaging configuration. The lower part of Fig. 2a depicts the dispersion relation of the lower polariton branch, resulting from the coupled TMDC monolayer–microcavity resonance. The energy of the picosecond pulsed laser was chosen as 1.6714 eV to achieve a compromise between signal strength and accessibility of the energy range. The excitation power was set well below threshold.

The photoluminescence map features two curved dispersion relations. However, only the low-energy branch can be detected on the position of the monolayer, whereas the higher-energy luminescence (1.65 eV at $k_{\parallel} = 0$) persists at sample positions in the periphery of the monolayer crystal (Supplementary Fig. 3). Thus, we conclude that the high-energy branch arises from luminescence of the uncoupled photonic resonance defined by the optical microcavity. From a

reference sample without the top DBR (see Supplementary Fig. 4), we can accurately determine the spectral position of the absorption of the MoSe₂ monolayer/hBN stack (1.660 eV). We fit the lower polariton branch (LPB in Fig. 2a) in the framework of a standard coupled oscillator approach (Supplementary Section 1). The model yields a normal-mode-splitting of 25 ± 2 meV, which is in general agreement with earlier reports on strongly coupled MoSe₂–cavity structures^{14,16,26}. Indeed, alongside the profound absorption feature from the MoSe₂ exciton, we find indications of absorption from the upper polariton branch in photoluminescence excitation measurements (Fig. 2b). We note that no important absorption is detected from the doped GaAs QW to the polaritonic state (horizontal dot-dashed lines in Fig. 2b indicate the resonance energies of the QW, the upper polariton and the MoSe₂ exciton). In addition, from a momentum-resolved photoluminescence experiment with 6 mW of continuous-wave excitation at 1.705 eV (Fig. 2a, top), we clearly observe the crossing (and no coupling) of the QW luminescence peak with the empty cavity dispersion branch.

This demonstrates that the GaAs QW does not contribute to the strong coupling and, in contrast to earlier works discussing hybrid TMDC–QW polaritons¹⁹, this polaritonic state solely emerges from the strong coupling conditions between the MoSe₂ monolayer and the cavity mode.

Condensation threshold

The high-density behaviour of our device is captured in Fig. 3, where we study its non-linear input–output characteristic. For this pump power dependence measurement, excitement is achieved with linearly polarized picosecond laser pulses at a repetition rate of 80 MHz. The laser is tuned to an energy of 1,671.4 meV (~40 meV above the emission of the lower polariton branch) to overlap with the upper polaritonic mode. In Fig. 3a–c, we show the dispersion relation maps below (Fig. 3a) and above (Fig. 3b,c) the condensation threshold; the relative false-colour scale of the maps reveals a strong non-linear increase of the emission at the threshold power of 14 mW. This power density corresponds to an injected density of electron–hole pairs of $\sim 3 \times 10^{12} \text{ cm}^{-2}$ (Supplementary Section 7) and thus occurs below the Mott density of excitons in MoSe₂ monolayers¹⁰.

The full pump power dependence is represented in Fig. 3d, where the photoluminescence of the dispersion relation has been

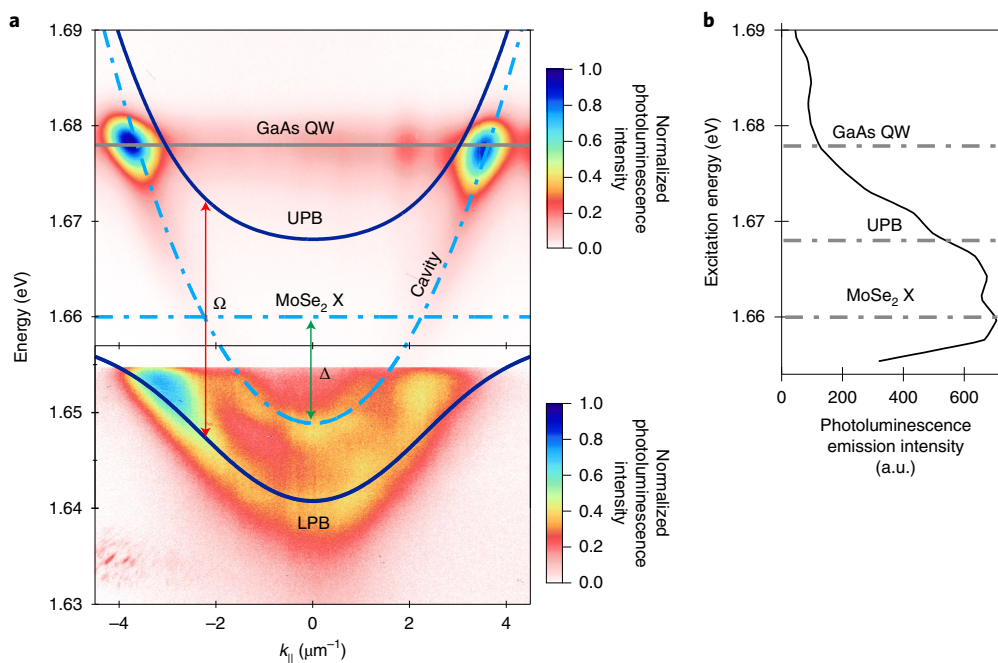


Fig. 2 | Optical properties of TMDC polaritons. **a**, Dispersion relation of the sample, showing the lower (LPB) and upper (UPB) polariton branches, MoSe₂ exciton and cavity modes, and the GaAs QW. The upper part (from 1.657 eV) of the figure is recorded under continuous-wave excitation with an energy of 1.705 eV. For the lower part (below 1.657 eV), the excitation is changed to picosecond pulses tuned at 1.6714 eV. For the sake of clarity, the intensity scale is normalized separately for both images. Ω and Δ indicate the normal-mode Rabi splitting and the photon-exciton energy detuning, respectively. **b**, Photoluminescence emission intensity of the lower polariton branch as a function of the energy of the continuous-wave excitation laser. Remarkably, the emission only increases for excitation energies below the QW resonance, demonstrating that there is no substantial coupling between the QW and the polariton system.

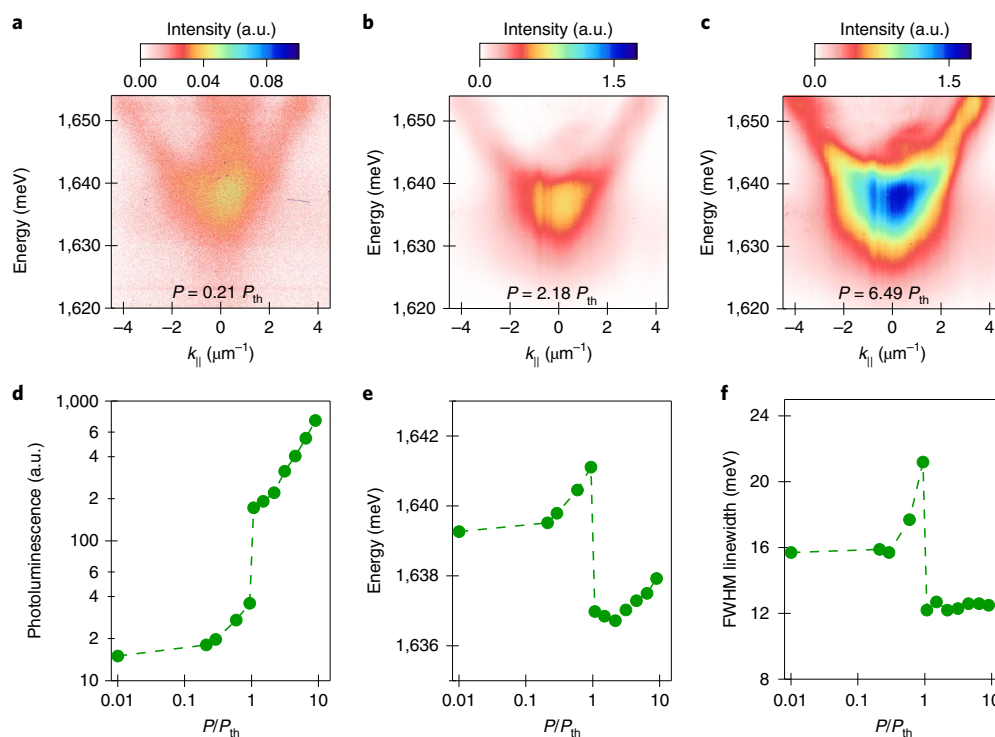


Fig. 3 | Non-linear polariton emission and emission intensity versus pump power. **a-c**, Polariton dispersion relation maps encoded in a false-colour scale for pump powers (P) of $0.21P_{th}$ (**a**), $2.18P_{th}$ (**b**) and $6.49P_{th}$ (**c**). **d-f**, Integrated photoluminescence (logarithmic scale) (**d**), energy of emission (**e**) and linewidth (**f**) as a function of pump power (logarithmic scale).

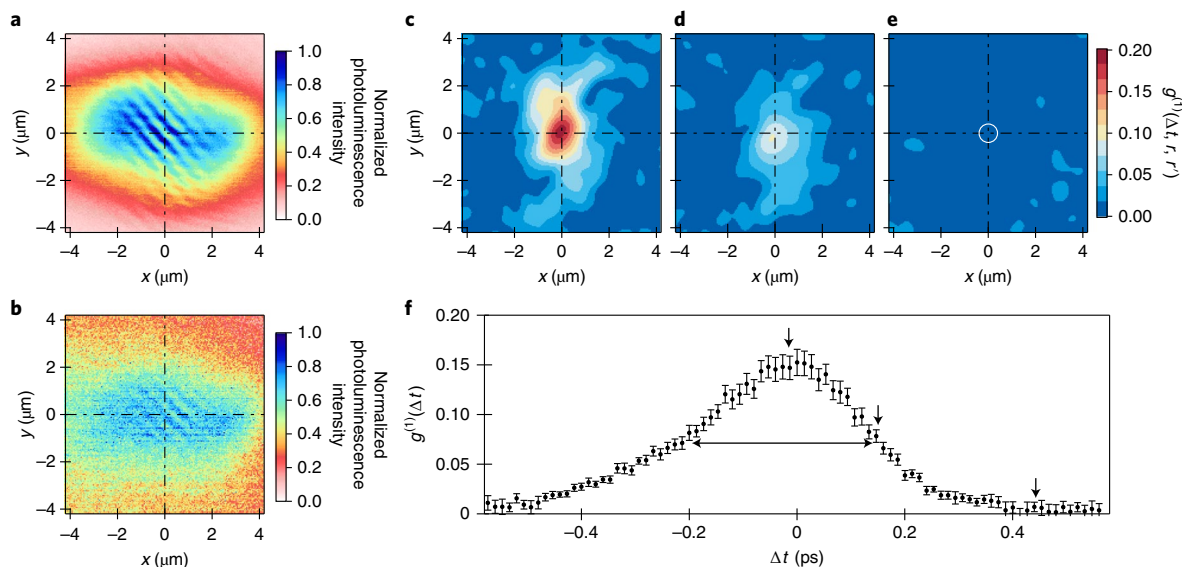


Fig. 4 | First-order autocorrelation measurement of the polariton condensate. **a, b**, Real space distribution of the polariton emission interference at zero delay at $9P_{\text{th}}$ (**a**) and $0.2P_{\text{th}}$ (**b**). **c–e**, Real space distribution of the first-order correlation function ($g^{(1)}$) for delays of 0 ps (**c**), 0.15 ps (**d**) and 0.42 ps (**e**) (same excitation conditions as **a**). **f**, $g^{(1)}$ versus delay between the interferometric arms; the value of $g^{(1)}$ is the average value within the white circle depicted in **e**, and the error bars correspond to the mean standard deviation. Vertical black arrows highlight the delays of the $g^{(1)}$ maps represented in **c–e**; the horizontal arrow indicates the temporal coherence length at half maximum of the $g^{(1)}$ function.

integrated for each power, providing the characteristic representation of the polariton non-linear threshold. (It should be noted that both vertical and horizontal axes are on a logarithmic scale and the emission intensity increase between the two pump powers immediately below and above the threshold is by more than a factor of 4.)

In Fig. 3e we plot the extracted peak energy as a function of the pump power. At threshold, we observe a notable jump of the peak position by -5 meV. This strongly suggests that our condensate is formed in a localized state of lower energy, which is induced by disorder or inhomogeneous strain in our system, as corroborated by the emergent real-space pattern of our condensate plotted in Supplementary Fig. 4. Such behaviour is well understood and indeed commonly observed in disordered microcavities²⁷, structured cavities^{28,29} and devices comprising strain traps³⁰. Furthermore, the lower polariton mode displays a blueshift above threshold, which amounts to ~ 2 meV as determined by analysing the statistical maximum of the luminescence peak. However, we note that this mode has a distinct substructure, which most likely arises from spatial sample inhomogeneities. As we show in Supplementary Fig. 8, this substructure of the peak results in an overestimated blueshift, such that the magnitude of 2 meV can only serve as an upper boundary.

The overall emission linewidth of the photoluminescence is depicted in Fig. 3f. Notably, we observe an increase in the emission linewidth towards the threshold, followed by a sudden drop at threshold to a value of ~ 12 meV. Indeed, this value remains constant with increasing pump power, which indicates that it is intrinsically limited by sample disorder and does not reflect the temporal coherence properties of the device emission. This is further evidenced by a large deviation of the spectral shape of the emission from a Lorentzian shape above the threshold.

Polariton coherence

One of the most important properties in a macroscopic condensed state is the emergence of spatially extended phase coherence. The degree of spatial coherence can be investigated via self-interfering the polariton emission in a Michelson interferometer. In such an interferometer, the relative temporal delay between the arms can be tuned within the timescale of the polariton emission lifetime, and

where one of the arms contains a retroreflector, this can invert both spatial axes of the reflected image.

With a cavity quality factor of ~ 500 (as a lower bound) and the emission characteristics of our TMDC excitons (~ 390 fs lifetime³¹), we expect a subpicosecond polariton lifetime of ~ 210 fs. The zero-delay calibration of the interferometer is initially set using the pulsed laser. This allows us to retrieve the corresponding zero delay of the polariton emission. Initially, we record the real space interferograms of the polariton emission above and below threshold (Fig. 4a,b, corresponding to $9P_{\text{th}}$ and $0.2P_{\text{th}}$, respectively, where P_{th} is the threshold pump power) at zero delay, with retroreflected images and displaced by $2 \mu\text{m}$. An extended interference pattern appears above threshold (Fig. 4a), and is several times larger than the pump spot (which has a full width at half maximum (FWHM) of $\sim 2 \mu\text{m}$). However, below threshold (Fig. 4b) we barely observe interference fringes because no macroscopic coherence is formed.

The Fourier transform analysis of such interferograms, combined with the intensity maps of each interferometer arm, allows us to reconstruct the real space distribution of the first-order coherence, also known as the $g^{(1)}(\Delta t)$ function. This analysis is shown in Fig. 4c–e, where we present different $g^{(1)}$ distributions as a function of three different temporal delays (0, 0.15 and 0.42 ps, respectively). The pump power is kept at $9P_{\text{th}}$. The $g^{(1)}$ map shown in Fig. 4c corresponds to the interferogram displayed in Fig. 4a.

We systematically measure the polariton $g^{(1)}$ maps versus delay in a temporal window of 1 ps around zero delay. From these maps, we extract the averaged $g^{(1)}$ value in a $1\text{-}\mu\text{m}$ -diameter circle around the origin of coordinates (indicated by the white circle in Fig. 4e) and plot it versus the delay (Fig. 4f). We observe a temporal Gaussian profile with a coherence time (FWHM) of 360 ± 10 fs, which, as expected for the case of pulsed excitation, is of the same order of magnitude as the previously indicated polariton lifetime of the system^{32,33}.

Valley control of TMDC polaritons

In MoSe_2 monolayers, the K and K' valleys with opposite spins are non-degenerate due to the lack of an inversion centre. This causes the spin of an exciton to be intrinsically locked to the corresponding

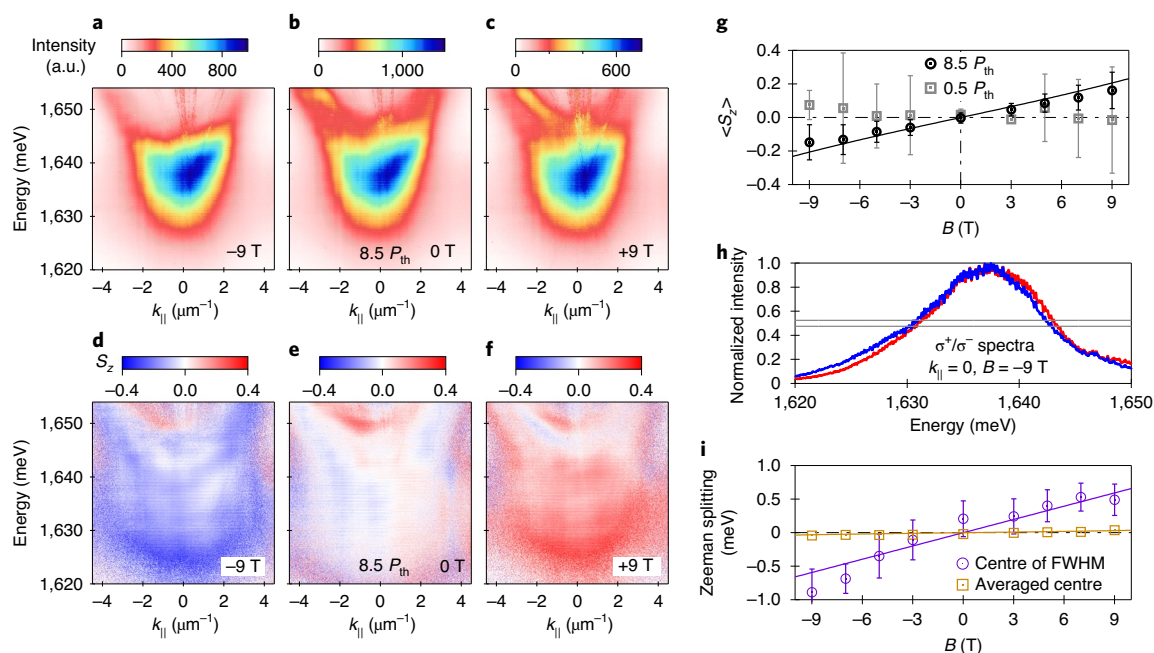


Fig. 5 | Dispersion relation and circular degree of polarization under strong magnetic fields. a–f, Maps of $I_{\sigma^+} + I_{\sigma^-}$ photoluminescence intensity (**a–c**) and degree of circular polarization, S_z (**d–f**), as a function of energy and momentum (k_{\parallel}) of the polariton condensate under a pump power of $8.5P_{th}$, encoded in two different colour scales, respectively, under magnetic fields of -9 T (**a,d**), 0 T (**b,e**) and 9 T (**c,f**). **g,** Spectrally averaged value of S_z at $k_{\parallel}=0$ (black circles) as a function of magnetic field under a pump power of $8.5P_{th}$. The corresponding values for S_z at a pump power of $0.5P_{th}$ are shown as grey squares (Supplementary Fig. 9). The error bars correspond to the mean standard deviation of each spectrally averaged S_z value. **h,** Normalized σ^+/σ^- spectra in red/blue at $k_{\parallel}=0$ and a magnetic field of -9 T. The horizontal grey lines at half maximum highlight the spectral shift between σ^+/σ^- detections. The energy shift between σ^+/σ^- FWHMs is used to extract the Zeeman splitting represented by purple open circles. **i,** Extracted Zeeman splitting under two different criteria: energy splitting of the normalized σ^+/σ^- spectra at FWHM (purple circles) and energy splitting extracted from the averaged centre of the intensity of σ^+/σ^- spectra at $k_{\parallel}=0$ (yellow squares) (see Supplementary Fig. 5 for further details). The error bars in the average centre criterion (yellow squares) are not visible. The error bars in the FWHM centre criterion are proportional to the noise in the normalized σ^+/σ^- spectra. The full lines in **g** and **i** are theoretical predictions from the model described in Supplementary Section 2.

valley, opening up the possibility to manipulate the valley degree of freedom by means of optical injection, as well as by built-in and external magnetic fields. Valley polarization therefore manifests in the increase in the degree of circular polarization of the device emission. In Fig. 5 we study the response of our polaritonic condensate in the presence of a vertical external magnetic field. By injecting the condensate ($\sim 8.5P_{th}$) with a linearly polarized laser, we ensure a balance between K and K' polaritons at zero magnetic field.

Figure 5a–c depicts dispersion relations recorded at -9 , 0 and 9 T for a constant pump power of 120 mW. Despite the observation of an increase of the condensation threshold with applied magnetic field, similar to previous reports of GaAs polariton condensates³⁴, our pump power was sufficiently strong to remain in the non-linear regime of bosonic condensation throughout the entire experimental series. In Fig. 5d–f, we plot the degree of circular polarization (S_z) for the corresponding magnetic fields. The maps of S_z distribution along the lower polariton branch display a notable change from negative to positive values while the magnetic field varies from -9 to 9 T. In the extreme cases (Fig. 5d,f), both S_z maps show an inhomogeneous distribution arising from the wide linewidth of the polariton emission (~ 12 meV), with predominantly higher S_z values for lower energies, where the energy splitting between σ^+ and σ^- populations becomes more evident.

A systematic variation of the external magnetic field displays progressive valley polarization of the polaritonic condensate in Fig. 5g. Averaging S_z at $k_{\parallel}=0$, in the range of energies $1,620$ – $1,650$ meV, we retrieve a clear linear variation of $\langle S_z \rangle$ as a function of magnetic field (black circles). For the sake of comparison, we include in the

same panel the corresponding analysis for a pump power of $0.5P_{th}$ (grey squares). The error bars in both cases correspond to the standard deviation of the spectrally averaged value of S_z . Interestingly, the below-threshold behaviour does not show a strong magnetic field dependence, having a greater error than the $\langle S_z \rangle$ value itself (Supplementary Section 6.1). This hints at the acceleration of polariton scattering via final state stimulation above threshold conditions, which in part prevents the rapid valley depolarization in the linear regime.

In Fig. 5h,i we investigate the energy splitting of the polariton resonance in the presence of the magnetic field. Due to the intrinsically broad spectrum of the polariton cloud and its complex shape, the extraction of the Zeeman splitting of the σ^+/σ^- emission requires some careful analysis.

First we compare the normalized σ^+/σ^- spectra at $k_{\parallel}=0$ at different magnetic field strengths, B (see Fig. 5h where we show the particular case of $B=-9$ T). While the maximum value of these σ^+/σ^- spectra only displays a small shift in energy, we notice a clear lateral offset of the spectra in their intensity wings. We extract the energy splitting from the energy difference between centres of the FWHM of each σ^+/σ^- spectra. The grey lines at 0.5 normalized intensity highlight the region where the blue and red curves are shifted in energy by ~ 1 meV. Applying the same analysis for all the measured magnetic field values, we retrieve the Zeeman splitting depicted in purple circles in Fig. 5i, where the fitted slope (full purple line) is 0.078 ± 0.008 meV T⁻¹.

The magnetic-field-induced splitting can be related to the exciton g factor via the expression $E_{\sigma^+} - E_{\sigma^-} = -|X|^2 g \mu_B B$, where $g \mu_B B$

is the splitting strength of the reservoir excitons, with g denoting the excitonic g factor, and $|X|^2$ the excitonic fraction of the lower polariton branch, which in our case is 30% at $k_{\parallel}=0$ (given the negative detuning and Rabi splitting previously discussed in Fig. 1); μ_B is the Bohr magneton. From the slope in Fig. 5i, we obtain an exciton g factor of 4.5 ± 0.5 , which is in good agreement with previously reported values for MoSe_2 excitons³⁵.

We notice that a peak analysis based on evaluating the statistical centre of each normalized σ^+/σ^- spectra yields a Zeeman splitting, yet with a slope ~ 20 times smaller (yellow squares in Fig. 5i). This method, being more punitive when applied to signals of complex shape (as in our case), serves as a lower bound for the estimate of the magnetic field splitting of our polariton condensate.

To support our experimental findings, we provide a simulation of the effect of the external magnetic field on the degree of circular polarization of polaritons. We use the model proposed in ref.³⁶ which is based on the system of semiclassical rate equations for the occupations of the condensed and non-condensed polariton states taking into account their spin polarization (Supplementary Section 2). The lines in Fig. 5g,i, fitting the experimental data, are consistent with the theory, which confirms the build-up of the circular polarization of the polariton state in the presence of a magnetic field accounting for the spin relaxation and stimulated scattering processes. In addition, as detailed in Supplementary Section 2.2, we can also capture the observed spin polarization by analysing the free energy of the polariton condensate in a trap of 5 meV depth.

Conclusions

We have demonstrated the bosonic condensation of exciton–polaritons formed from strong coupling between monolayer MoSe_2 excitons and a microcavity–photonic field. The input–output response of the system reveals a clear switching threshold, with a sudden increase in the non-linear emission, linewidth narrowing and a slight blueshift of emission energies above threshold, all of which highlight the emergence of polariton lasing. The first-order coherence function of the emission shows a macroscopically extended common phase, which expands up to $4\mu\text{m}$ in our sample, and a coherence time of the same order of magnitude as the polariton lifetime. In the presence of an externally applied magnetic field, we demonstrate the lifting of the valley degeneracy of the condensed state, and the valley polarization of the system.

We believe that the giant exciton binding energies provided by TMDC layers will allow the observation of spatially and temporally coherent valley condensates at ambient conditions in carefully adapted devices. It is reasonable to assume that the increased photoluminescence of tungsten-based TMDCs at room temperature³⁷, in conjunction with cavities featuring improved quality factors, can provide a feasible pathway towards such a demonstration. In conjunction with recently developed technologies for large-scale monolayer growth and electrical injection^{38,39}, this will represent an entirely new platform for coherent light-sources based on bosonic stimulation. The capability to address and manipulate the valley index of the condensate makes our system highly promising for the exploration of large-scale coherent valley currents based on liquid light.

Online content

Any methods, additional references, Nature Research reporting summaries, source data, extended data, supplementary information, acknowledgements, peer review information; details of author contributions and competing interests; and statements of data and code availability are available at <https://doi.org/10.1038/s41563-021-01000-8>.

Received: 24 September 2020; Accepted: 31 March 2021;
Published online: 6 May 2021

References

- Anderson, M. H., Ensher, J. R., Matthews, M. R., Wieman, C. E. & Cornell, E. A. Observation of Bose–Einstein condensation in a dilute atomic vapor. *Science* **269**, 198–201 (1995).
- Ketterle, W. & van Druten, N. J. Bose–Einstein condensation of a finite number of particles trapped in one or three dimensions. *Phys. Rev. A* **54**, 656 (1996).
- Ketterle, W. Nobel lecture: when atoms behave as waves: Bose–Einstein condensation and the atom laser. *Rev. Mod. Phys.* **74**, 1131–1151 (2002).
- Kasprzak, J. et al. Bose–Einstein condensation of exciton polaritons. *Nature* **443**, 409–414 (2006).
- Imamoğlu, A., Ram, R. J., Pau, S. & Yamamoto, Y. Nonequilibrium condensates and lasers without inversion: exciton–polariton lasers. *Phys. Rev. A* **53**, 4250–4253 (1996).
- Deng, H., Weihs, G., Snoke, D., Bloch, J. & Yamamoto, Y. Polariton lasing vs photon lasing in a semiconductor microcavity. *Proc. Natl Acad. Sci. USA* **100**, 15318–15323 (2003).
- Carusotto, I. & Ciuti, C. Quantum fluids of light. *Rev. Mod. Phys.* **85**, 299–366 (2013).
- Weisbuch, C., Nishioka, M., Ishikawa, A. & Arakawa, Y. Observation of the coupled exciton–photon mode splitting in a semiconductor quantum microcavity. *Phys. Rev. Lett.* **69**, 3314–3317 (1992).
- Schneider, C., Glazov, M. M., Korn, T., Höfling, S. & Urbaszek, B. Two-dimensional semiconductors in the regime of strong light–matter coupling. *Nat. Commun.* **9**, 2695 (2018).
- Wang, G. et al. Colloquium: excitons in atomically thin transition metal dichalcogenides. *Rev. Mod. Phys.* **90**, 021001 (2018).
- Lundt, N. et al. Room-temperature Tamm–plasmon exciton–polaritons with WSe_2 monolayer. *Nat. Commun.* **7**, 13328 (2016).
- Liu, X. et al. Strong light–matter coupling in two-dimensional atomic crystals. *Nat. Photon* **9**, 30–34 (2015).
- Flatten, L. C. et al. Room-temperature exciton–polaritons with two-dimensional WS_2 . *Sci. Rep.* **6**, 33134 (2016).
- Dufferwiel, S. et al. Exciton–polaritons in van der Waals heterostructures embedded in tunable microcavities. *Nat. Commun.* **6**, 8579 (2015).
- Lundt, N. et al. Optical valley Hall effect for highly valley-coherent exciton–polaritons in an atomically thin semiconductor. *Nat. Nanotechnol.* **14**, 770–775 (2019).
- Dufferwiel, S. et al. Valley-addressable polaritons in atomically thin semiconductors. *Nat. Photon* **11**, 497–501 (2017).
- Gu, J. et al. Enhanced nonlinear interaction of polaritons via excitonic Rydberg states in monolayer WSe_2 . *Nat. Commun.* **12**, 2269 (2021).
- Stepanov, P. et al. Exciton–exciton interaction beyond the hydrogenic picture in a MoSe_2 monolayer in the strong light–matter coupling regime. *Phys. Rev. Lett.* **126**, 167401 (2021).
- Emmanuele, R. P. A. et al. Highly nonlinear trion–polaritons in a monolayer semiconductor. *Nat. Commun.* **11**, 3589 (2020).
- Wang, Z. et al. Evidence of high-temperature exciton condensation in two-dimensional atomic double layers. *Nature* **574**, 76–80 (2019).
- Malpuech, G., Kavokin, A., Di Carlo, A. & Baumberg, J. J. Polariton lasing by exciton–electron scattering in semiconductor microcavities. *Phys. Rev. B* **65**, 153310 (2002).
- Bajoni, D. et al. Dynamics of microcavity polaritons in the presence of an electron gas. *Phys. Rev. B* **73**, 205344 (2006).
- Tan, L. B. et al. Interacting polaron–polaritons. *Phys. Rev. X* **10**, 021011 (2020).
- Castellanos-Gomez, A. et al. Deterministic transfer of two-dimensional materials by all-dry viscoelastic stamping. *2D Mater.* **1**, 011002 (2014).
- Richard, M., Kasprzak, J., Romestain, R., André, R. & Dang, L. S. Spontaneous coherent phase transition of polaritons in CdTe microcavities. *Phys. Rev. Lett.* **94**, 187401 (2005).
- Dufferwiel, S. et al. Valley coherent exciton–polaritons in a monolayer semiconductor. *Nat. Commun.* **9**, 4797 (2018).
- Kulakovskii, V. D. et al. Bose–Einstein condensation of exciton polaritons in high-Q planar microcavities with GaAs quantum wells. *JETP Lett.* **92**, 595–599 (2010).
- El Daif, O. et al. Nonlinear relaxation of zero-dimension-trapped microcavity polaritons. *Appl. Phys. Lett.* **92**, 081910 (2008).
- Adiyatullin, A. F. et al. Periodic squeezing in a polariton Josephson junction. *Nat. Commun.* **8**, 1329 (2017).
- Balili, R., Hartwell, V., Snoke, D., Pfeiffer, L. & West, K. Bose–Einstein condensation of microcavity polaritons in a trap. *Science* **316**, 1007–1010 (2007).
- Jakubczyk, T. et al. Radiatively limited dephasing and exciton dynamics in MoSe_2 monolayers revealed with four-wave mixing microscopy. *Nano Lett.* **16**, 5333–5339 (2016).
- Daskalakis, K. S., Maier, S. A. & Kéna-Cohen, S. Spatial coherence and stability in a disordered organic polariton condensate. *Phys. Rev. Lett.* **115**, 035301 (2015).
- De Giorgi, M. et al. Interaction and coherence of a plasmon–exciton polariton condensate. *ACS Photonics* **5**, 3666–3672 (2018).

34. Yakovlev, D. R. et al. Combined exciton-cyclotron resonance in quantum well structures. *Phys. Rev. Lett.* **79**, 3974–3977 (1997).
35. Koperski, M. et al. Orbital, spin and valley contributions to Zeeman splitting of excitonic resonances in MoSe₂, WSe₂ and WS₂ monolayers. *2D Mater.* **6**, 015001 (2018).
36. Lundt, N. et al. Magnetic-field-induced splitting and polarization of monolayer-based valley exciton polaritons. *Phys. Rev. B* **100**, 121303 (2019).
37. Wang, G. et al. Spin-orbit engineering in transition metal dichalcogenide alloy monolayers. *Nat. Commun.* **6**, 10110 (2015).
38. Schneider, C. et al. An electrically pumped polariton laser. *Nature* **497**, 348–352 (2013).
39. Gu, J., Chakraborty, B., Khatoniar, M. & Menon, V. M. A room-temperature polariton light-emitting diode based on monolayer WS₂. *Nat. Nanotechnol.* **14**, 1024–1028 (2019).

Publisher's note Springer Nature remains neutral with regard to jurisdictional claims in published maps and institutional affiliations.

© The Author(s), under exclusive licence to Springer Nature Limited 2021, corrected publication 2021

Methods

We use an optical setup in which both spatially (near-field) and momentum-space (far-field) resolved spectroscopy and imaging are accessible. Various laser sources are coupled into the beam-path, including a 532 nm continuous-wave laser, and a wavelength-tunable system composed of a titanium sapphire laser (10 ps pulse length). For imaging the sample, as well as for white-light reflection spectroscopy, we utilize a thermal light-source. Our setting allows us to access both the spatial and angular distribution of the emitted signal from the sample. To obtain a spatially resolved signal, the emission from the sample is simply projected onto the imaging plane of the spectrometer in a conventional microscope configuration. For this purpose, a Peltier-cooled silicon charge-coupled device camera with a resolution of $1,024 \times 1,024$ pixels is coupled to the spectrometer.

To resolve the momentum-space distribution of the emission (Fourier space imaging) an additional lens is placed into the beam path, where its distance to the back focal plane of the objective is equal to its focal length. The angular resolution of the system is $\sim 0.03 \mu\text{m}^{-1}$ ($\sim 0.2^\circ$). For all the experiments reported here, the sample was mounted in a closed-cycle cryostat providing magnetic fields up to 9 T and sample temperatures down to ~ 4 K, and the photoluminescence is collected through a 0.81 numerical aperture microscope objective.

The spatial-temporal coherence measurements are done in a Michelson interferometer. One retroreflector in one of the interferometric arms inverts vertically and horizontally the spatial coordinates of one of the images. The other interferometer arm is mounted on a nanometric translation stage that allows the relative temporal delay between the two arms to be controlled accurately. The two interference images are superimposed at a chosen angle in the detection charge-coupled device, forming an interfering pattern in real space.

Data availability

The experimental data that support the findings of this study are available in figshare with the identifier <https://doi.org/10.6084/m9.figshare.14342471>.

Acknowledgements

This work was funded by the Deutsche Forschungsgemeinschaft (DFG, German Research Foundation)–INST 93/932-1 FUGG. The authors gratefully acknowledge funding by the State of Bavaria and Lower Saxony. Funding provided by the European

Research Council (ERC project 679288, unlimit-2D) is acknowledged. T.H.H., S.K. and S.H. acknowledge financial support by DFG through the Würzburg-Dresden Cluster of Excellence on Complexity and Topology in Quantum Matter “ct.qmat” (EXC 2147, project-id 390858490). T.H.H. acknowledges funding by the doctoral training program ‘Elitenetzwerk Bayern’ and support by the German Academic Scholarship Foundation. S.T. acknowledges funding from NSF DMR 1955889, DMR 2111812, DMR 1933214 and 1904716. S.T. also acknowledges DOE-SC0020653. E.S. and A.V.K. acknowledge Westlake University (project number 041020100118) and Program 2018R01002 funded by the Leading Innovative and Entrepreneur Team Introduction Program of Zhejiang. K.W. and T.T. acknowledge support from the Elemental Strategy Initiative conducted by the MEXT, Japan, grant number JPMXP0112101001, JSPS KAKENHI grant number JP20H00354 and the CREST (JPMJCR15F3), JST. A.V.K. acknowledges the St Petersburg State University for research grant number 73031758.

Author contributions

The experiments were performed by C.A.-S. and M.W., with contributions from M.K. and T.H.H. The data analysis was performed by C.A.-S. and M.W., with contributions from T.H.H., S.K. and C.S. The Epi wafer was designed by C.S. and S.H., and grown by H.S. The device was built by M.W. Crystals were provided and customized by H.C., S.T., K.W. and T.T. The theory and simulations were performed by E.S. and C.S. with contributions from C.A.-S. and with the supervision of A.V.K. The project was supervised by C.S. All the authors participated in the writing of the manuscript.

Competing interests

The authors declare no competing interests.

Additional information

Supplementary information The online version contains supplementary material available at <https://doi.org/10.1038/s41563-021-01000-8>.

Correspondence and requests for materials should be addressed to C.A.-S., S.T. or C.S.

Peer review information *Nature Materials* thanks the anonymous reviewers for their contribution to the peer review of this work.

Reprints and permissions information is available at www.nature.com/reprints.